Functionally grading the shape memory response in NiTi films: Laser irradiation

A. J. Birnbaum,[a] G. Satoh, and Y. L. Yao
Department of Mechanical Engineering, Columbia University, New York, New York 10027, USA

(Received 25 February 2009; accepted 24 June 2009; published online 18 August 2009)

A new process and mechanism are presented for controlling the shape memory response spatially within monolithic NiTi thin film structures. This technique is shown to effectively control the martensitic phase transformation temperature and exhibits control over aspects of the mechanical and shape memory responses as well. Specifically, the martensitic phase transformation temperature decreases with incident laser energy density. Concomitant modifications are observed in both the mechanical and shape memory responses in laser processed films. Analysis and characterization are performed via temperature controlled optical microscopy, x-ray diffraction, atomic force microscopy, and nanoindentation. © *2009 American Institute of Physics*. [DOI: 10.1063/1.3183950]

I. INTRODUCTION

Despite the technological challenges that arise from their inherent complexity, shape memory materials continue to receive a great deal of interest and attention due to their vast potential for both active and passive applications. The past decade has seen a surge in research directed toward gaining a deeper understanding of an array of metallic and polymer based material systems over multiple length scales. Microscale structures, specifically silicon wafer based thin film configurations, have been of particular interest due to the maturity of planar based microelectromechanical system (MEMS) fabrication techniques as well as enhancements in material performance due to excellent inherent scalability. Countless studies have also gone into characterizing many of the parameters affecting the resulting structure and performance of these films and devices. These include, but are not limited to, deposition process,[1,2] crystallization technique,[3,4] annealing parameters,[5,6] and fabrication process.[7,8]

It is interesting to note, however, that the vast majority of these studies are limited to homogeneous shape memory structures. In this context, the term homogeneous is meant to suggest homogeneous shape memory characteristics, i.e., phase transformation temperature, strain recovery via the shape memory effect (SME) or superelastic effect (SE), etc. That is not to suggest that the topic has been completely overlooked though. Much of the microscale work in this area concentrates either on through thickness compositional gradients, composite material layering, or surface treatment. Cole *et al.*[9] deposited titanium rich films onto nickel rich NiTi substrates followed by an anneal step allowing diffusion between the film and substrate, resulting in through thickness compositional gradients. Martins *et al.*[10] cosputtered NiTi films from an alloyed and elemental target, applying variable power to the elemental Ti target during deposition and again resulting in a compositional gradient through the film thickness. Fu and Du[11] deposited layers of titanium nitride on NiTi films in order to improve tribological performance, while Kim and Lee[12] prepared NiTi/PZT shape memory-piezoelectric thin film heterostructures. The investigations involving continuous through thickness compositional gradients were performed within the context of improving surface wear properties while maintaining the shape memory character of the film. This is in contrast to composite layered investigations such as that of Kim and Lee[12] which was focused on fabricating bimorph actuating devices.

The above mentioned studies do in fact address some central issues with regards to functional gradation; however, they are all limited to grading in one dimension, i.e., through the thickness. This is due to the process by which crystallization and annealing are performed. All of those studies rely on applying some uniform heat treatment to the entire film-substrate system. Recently, several investigations have been performed on thin film crystallization and annealing via local, selective laser irradiation. Wang and Bellouard *et al.*[13,14] crystallized amorphous, sputter deposited NiTi films via a continuous wave (cw) solid phase (no melting) crystallization scheme. Since all of the shape memory responses stem from the crystal structure of the austenite and martensite structures, only those regions selectively crystallized via the laser will exhibit these characteristics, while the amorphous matrix remains passive. He *et al.*[15] also performed cw solid phase crystallization via a CO_2 laser. These efforts may be seen as extending the concept of functional grading to a two-dimensional framework, in this case the plane of the film. Additionally, previous investigations by Birnbaum *et al.*[16,17] examined microstructural and phase consequences of the pulsed, melt-mediated process utilized here over an array of process conditions including incident laser fluence and preheated substrate temperature. Furthermore, the mechanical and shape memory responses of laser processed films were characterized via nanoindentation.

This work proposes a pulsed, melt-mediated laser crystallization process to produce functionally graded shape memory structures. This process not only provides spatial control over the presence of the shape memory response but, through proper use of operational parameters, can tailor the shape memory response itself, i.e., phase transformation tem-

[a]Electronic mail: andrew.birnbaum@gmail.com.

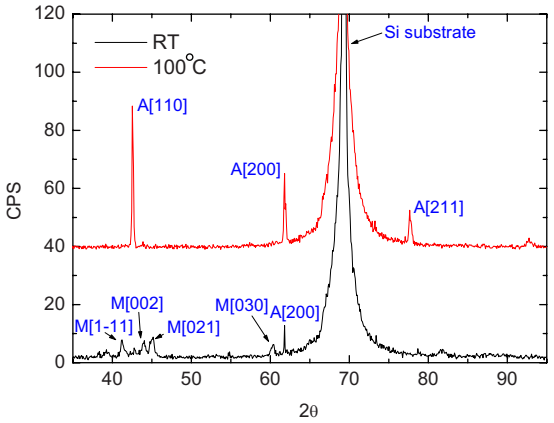

FIG. 1. (Color online) XRD spectra for the as-annealed NiTi film prior to laser processing confirming the film as fully martensitic at room temperature and transforms to austenite at elevated temperatures.

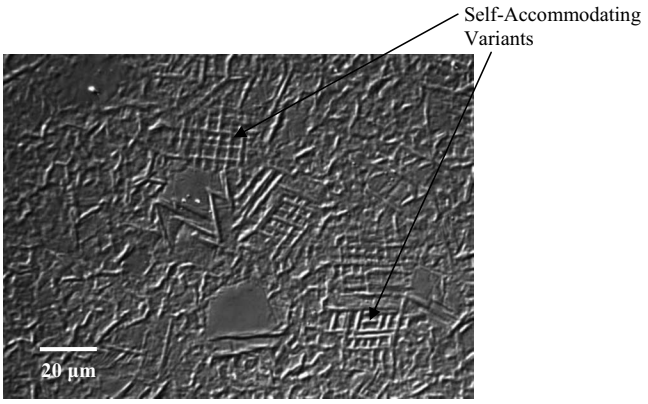

FIG. 2. Optical micrograph of surface of as-annealed film (room temperature). Note the self-accommodating nature of the martensitic variants.

perature, transformation strain, recovery stress, etc. Utilization of a pulsed process as opposed to a cw process presents the user with several distinct advantages. For example, the work presented recently by Wang *et al.*[18] shows a relatively large partially crystallized transition region between the fully crystallized portion of the film and the amorphous matrix. This transition zone is completely eliminated and extremely sharp boundaries are attainable due to the low pulse duration to thermal diffusivity time scales. Additionally, it is nearly impossible to control the extent of crystallization in the depth direction for a cw process. This study demonstrates the ability for very fine control over the depth that may be affected for a 1 μm film. Furthermore, this work seeks to provide a means for producing an entirely new class of monolithic shape memory MEMS structures that can be active over a predetermined set of temperature ranges. For example, one can envision a microfluidic system for laboratory on chip applications that may have a thermally induced shape memory actuator that responds over one set of temperatures and adjacent sets of pumps or valves that activate over different sets of temperature ranges.

II. EXPERIMENTAL SETUP

NiTi films were deposited by simultaneous cosputtering from an alloyed NiTi target and pure titanium target at powers of 302 and 50 W, respectively, for 300 s at an argon pressure of 3 mTorr resulting in films 1 μm in thickness. The films were deposited on a 1 μm ultralow residual stress silicon nitride (Si_3N_4) barrier layer that had been deposited on a [100] silicon wafer via low pressure chemical vapor deposition. The deposition was performed at room temperature, and thus resulted in an amorphous as deposited configuration. Films were subsequently annealed at 460 °C for 5 min in a vacuum furnace, resulting in fully crystalline films. The x-ray diffraction (XRD) spectra presented in Fig. 1 were taken at room temperature and 100 °C and confirm that the film is martensitic at room temperature and transforms to austenite at elevated temperatures. Figure 2 is an optical micrograph of the as-annealed film surface. Note the self-accommodating nature of the martensitic variants. Furthermore, the film composition as Ti-51.8 at. % was obtained via a calibrated electron microprobe. Additionally, residual stresses in the as-annealed film were measured via the wafer curvature method revealing a tensile stress of approximately 225 MPa at 100 °C while in the austenitic state.

Films were processed via pulsed irradiation using a 308 nm wavelength, XeCl excimer laser with 30 ns pulse duration over a wide range of incident laser energy densities. All results presented are for films that have been single-shot laser irradiated at fluencies ranging from approximately 600 to 1350 mJ/cm^2. Energy density was uniform within the irradiated region whose geometry was a square, 320 $\times$320 μm^2. The laser system is synchronized with the underlying *XYZ* motion system such that a series of energy densities may be applied producing a spatial array on a single specimen. Each square region is an irradiated area of a single uniform energy density with 10 μm spacing. Additionally, a 632 nm HeNe laser and photodiode were used *in situ* in order to capture the time resolved transient reflectance of the irradiated region for 0.5–2.0 GHz sampling rates.

III. THEORETICAL BACKGROUND

In order to successfully grade the shape memory response, a deep understanding of the physical parameters that govern the response itself is necessary. The transformation may be described thermodynamically via a Gibbs free energy formulation. Thus the near equilibrium transformation proceeds upon a decrease in total free energy, i.e., $\Delta G^{A\rightarrow M}<0$, and therefore $G^M_{\text{tot}}<G^A_{\text{tot}}$. The change in free energy is described as

$$\Delta G^{A\rightarrow M}=A\gamma+V\Delta G_{\text{strain}}-V\Delta G_V, \tag{1}$$

where A, γ, V, ΔG_{strain}, and ΔG_V are the interfacial area, interfacial free energy per unit area, volume, change in strain energy per unit volume, and change in volumetric free energy per unit volume, respectively. Thus for the austenite to martensite transformation to proceed, the formation of new interfaces as well as strain energy due to transformation acts to inhibit the transformation, while the change in volumetric free energy between the respective phases provides the necessary driving force. Therefore, for no externally applied stress, there exists an equilibrium temperature T_{eq} at which the volumetric free energies of the respective phases are

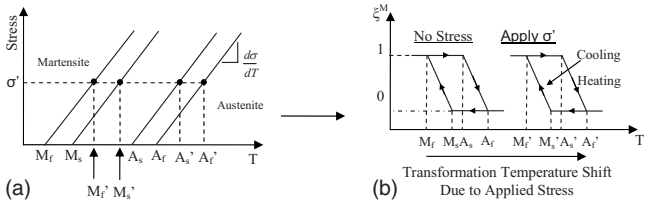

FIG. 3. (a) Stress-temperature phase diagram. (b) Volume fraction of martensite as a function of temperature for the unstressed and stressed cases.

equal. However, as stated above, additional driving force is necessary for the transformation to proceed, and thus the transformation actually requires some degree of supercooling. The transformation begins at temperature M_s below T_{eq}. Further supercooling is necessary for the transformation to continue in order to overcome the increase in energy caused by the formation of new austenite-martensite interfaces. It finally is completely transformed at M_f. The reverse martensite to austenite transformation proceeds similarly and starts and ends at A_s and A_f. The Gibbs free energy of the individual phases may be described as[19]

$$G = U + PV - TS - \sigma:\varepsilon, \tag{2}$$

where U, P, V, T, S, ε, and σ are the internal energy, pressure, volume, temperature, entropy, and strain, and stress (uniaxial), respectively. Also, at equilibrium (at a constant pressure):

$$G^M = G^A \Rightarrow H^A - T_{eq}S^A = H^M - T_{eq}S^M \Rightarrow \Delta S = \frac{\Delta H}{T_{eq}} \tag{3}$$

and

$$dG^M = dG^A \Rightarrow -S^A dT - \varepsilon^A d\sigma = -S^M dT - \varepsilon^M d\sigma. \tag{4}$$

Combining the results of Eqs. (3) and (4), one obtains a Clausius–Clapeyron-type equation:

$$\frac{d\sigma}{dT} = -\frac{\Delta S}{\varepsilon^t} = -\frac{\Delta H}{T_{eq}\varepsilon^t}, \tag{5}$$

where ε^t is the strain associated with the transformation. This relationship is central to the mechanism proposed for functionally grading the phase transformation temperature. In essence it describes the rate with which the equilibrium phase transformation temperatures for a given alloy composition change as a function of the stress state in the solid. Therefore, by locally controlling the stress state, one can effectively control the temperatures over which the phase transition will occur. Figures 3(a) and 3(b) depict this schematically.

IV. PROPOSED MECHANISM

It is well documented[20,21] that solid phase crystallization of sputter deposited NiTi films via furnace annealing results in significant tensile residual film stress upon cooling to room temperature. The residual stress is composed of components from intrinsic stress due to lattice mismatch at the film/barrier layer interface, thermal expansion coefficient mismatch, and volumetric contraction due to differences in molar volume between the amorphous and crystalline

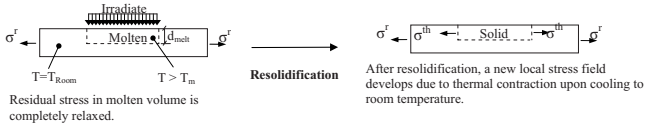

FIG. 4. Schematic detailing the melt and solidification process elucidating the mechanism by which the shape memory response is functionally graded.

phases.[21] It has been reported, however,[22,23] that the major contributor is the thermal stress developed upon cooling down, as the coefficient of thermal expansion of NiTi is as much as four times that of silicon and silicon nitride. Therefore, for a film of fixed composition, the resulting phase transformation temperatures will be shifted according to the residual stress state that develops in the film.

Figure 4 is a schematic representing a portion of the film undergoing laser irradiation, melting, and subsequent resolidification. Upon irradiation, a molten layer forms and the liquid solid interface propagates toward the film-barrier layer interface. There is in fact a range of laser energies that will result in ultimate melt depths less than that of the film thickness. This is termed partial melting. This study is restricted to incident laser energy densities that are below the film's complete melt threshold, i.e., the ultimate depth of melting, $d_{melt} < 1$ μm. See Ref. 17 for a full description of thin film melting regimes. Upon melting, the residual stresses in the molten region are completely relaxed. Vertical epitaxial regrowth from remaining crystals occurs upon reaching the equilibrium melting temperature until the entire molten region is again solid. The resolidified layer begins to cool, and upon doing so, develops a new stress field due to thermal contraction. The stresses that develop are proportional to the change in temperature between the equilibrium melting temperature and room temperature and are inversely proportional to the cross sectional area of the region, and therefore the ultimate depth of melting. A mechanism by which the phase transformation temperatures may be locally controlled via laser irradiation is proposed for the melted region, since $d_{melt} \sim E_{laser}$, $\sigma^m \sim 1/d_{melt}$, and $M_s \sim \sigma$:

$$M_s \sim \frac{1}{E_{laser}}. \tag{6}$$

The irradiated area of the film is confined to the desired geometry of the projection mask, and thus in-plane grading has been accomplished as well.

V. RESULTS AND DISCUSSION

A. Melting and solidification

An understanding of the melting and resolidification process, specifically the relationship between the laser energy density, is central in successfully predicting and spatially controlling phase transformation temperatures. As stated above, this study is restricted to ultimate melt depths less than that of the film thickness. Figures 5(a)–5(d) are several representative transient reflectance spectra obtained *in situ* during laser irradiation. Figure 5(a) is the actual temporal profile of the laser as captured by an additional photodiode. It is important to note that since the extinction depth $(1/e^2)$

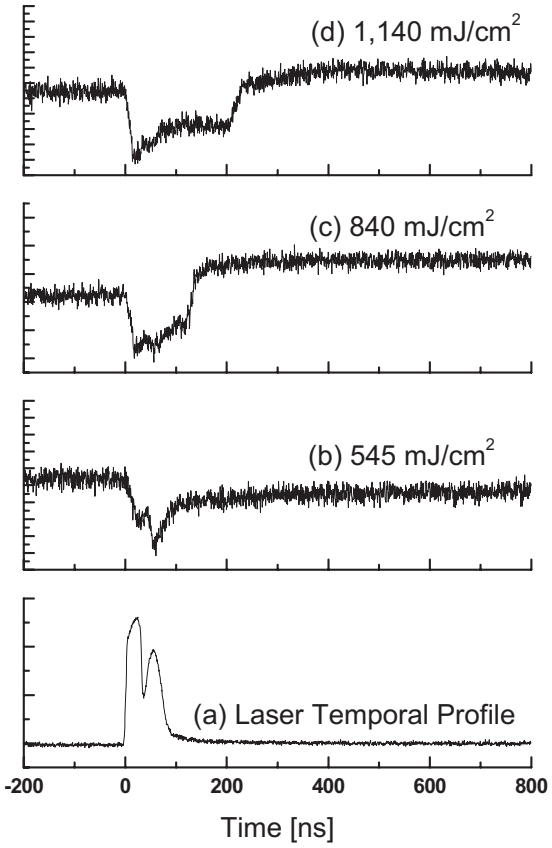

FIG. 5. Transient reflectance spectra using a 632 nm HeNe probe and photodiode obtained *in situ* during laser irradiation for (b) 545 mJ/cm^2, (c) 840 mJ/cm^2, (d) 1141 mJ/cm^2, and (e) 1140 mJ/cm^2. (a) The actual laser temporal profile was obtained via a different photodiode.

for NiTi is approximately 56 nm, the signal may be seen as a reflection exclusively from the film surface with essentially no volumetric interaction. For Figs. 5(b)–5(d), the initial reflectance ($t<0$) represents that of the solid, crystalline film. Upon irradiation a steep drop in reflected signal occurs representing surface melting. A subsequent plateau is observed, followed by a steep increase back to near the initial reflectivity value. The length of the plateau represents the time that the film surface remained molten. Figure 6 is a plot of melt duration as a function of energy density. A discontinuity in slope is observed at approximately 1350 mJ/cm^2. This discontinuity stems from the film having undergone complete, through thickness melting. Therefore, in order to solidify, nucleation must occur prior to grain growth. Nucleation requires significant undercooling and added time to reach these lower temperatures, and thus results in a significantly increased surface melt duration. An average interface velocity of 6.5 m/s may now be determined from this by assuming a sharp interface and traveled a total of 2 μm (melt and regrowth) in approximately 300 ns. If a constant average interface velocity is assumed for each irradiation, the energy density dependence of the melt depth may then be calculated. This is also plotted in Fig. 6.

B. Phase transformation temperatures

1. Surface versus volume

Phase transformation temperatures were characterized via *in situ* temperature controlled optical microscopy which

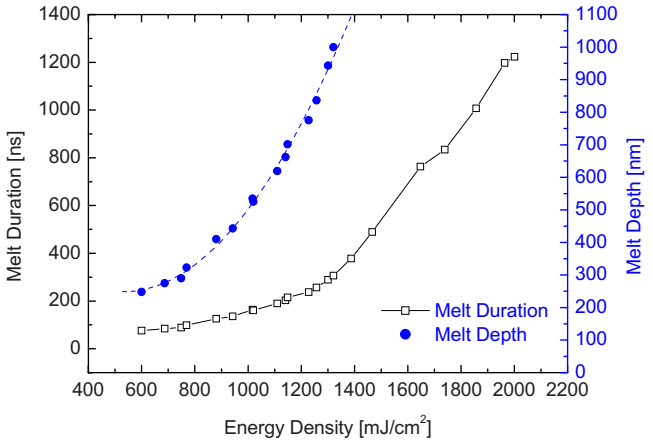

FIG. 6. (Color online) Plot of melt duration as a function of energy density as obtained via transient reflectance analysis. Also plotted is the melt depth vs energy density calculated based on a constant interface velocity of 6.5 m/s.

provides information regarding the transformation characteristics of the film surface and XRD which provides volumetric data. This is a particularly effective characterization scheme as two distinctive zones result from laser processing: the upper melted and resolidified region and the underlying unmelted portion of the film. Characterization of the as-annealed film (no laser processing) was performed in order to establish a baseline set of phase transformation parameters. Figures 7(a)–7(d), 8(a), and 8(b) are optical micrographs and XRD spectra upon heating and cooling. Note that the optical micrographs reveal (via visual inspection) the surface transformation (martensite to austenite) initiating at approximately A_s=45.1 °C. Full transformation is observed by A_f=59.0 °C, and the reverse transformation starts at M_s =41.6 °C and M_f=32.3 °C. Figures 8(a) and 8(b) are XRD spectra taken across the 2θ range where the [110] austenite peak is located. They reveal $A_s \approx 65$ °C, $A_f \approx 79$ °C, $M_s \approx 54$ °C, and $M_f \approx 43$ °C. The phase transformation temperatures differ by as much as 20 °C as observed by microscopy and XRD. Wu *et al.*[24] reported a substantial through thickness stress gradient in sputter deposited, furnace annealed NiTi films stemming from lattice mismatch at the film/barrier layer interface. The maximum stress is located at the interface and decreases monotonically as the traction-free film surface is approached. This stress gradient results in a corresponding gradient in phase transformation temperature,

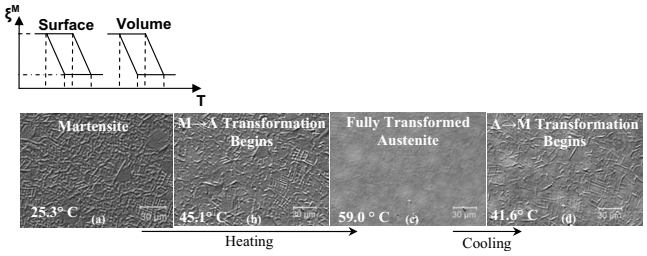

FIG. 7. As-annealed NiTi film (representative): (a) Fully martensitic at room temperature. (b) Upon heating, the martensite to austenite transformation begins for an A_s=45.1 °C. (c) The transformation is complete, A_f =59.0 °C, and (d) upon cooling, the martensite to austenite begins, M_s =41.6 °C.

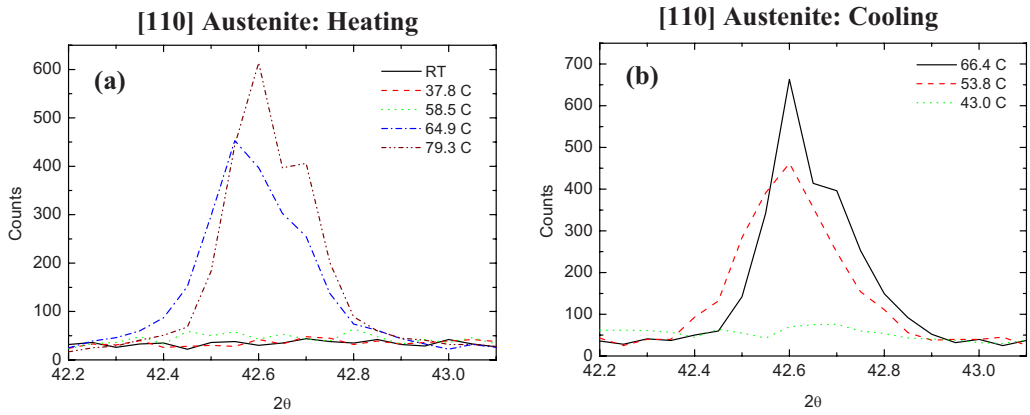

FIG. 8. (Color online) Typical XRD spectra collected from unprocessed, as-annealed film revealing the emergence and disappearance of the [110] austenite peak upon (a) heating and (b) cooling. The phase transformation temperatures are approximated as $A_s \approx 65$ °C, $A_f \approx 79$ °C, $M_s \approx 54$ °C, and $M_f \approx 43$ °C.

explaining the reduced phase transformation temperatures at the surface observed via microscopy relative to those obtained through XRD. This nonuniform behavior is detailed schematically in the inset in Fig. 7 where the ordinate is volume fraction of martensite and the abscissa the temperature. The inset reveals schematically that the phase transformation temperatures are higher within the "bulk" volume of the film than that of the surface where traction-free conditions are present.

2. Energy density effects

Figure 9 shows room temperature XRD spectra collected from films that have been laser processed at successively increasing laser energy densities. Note that the unprocessed films consist primarily of varying oriented martensite. However, upon laser processing over increasing energy densities, the [1–11] martensitic peak vanishes, while the [110] austenitic and [31–1] Ni_4Ti_3 peaks progressively emerge. Since there was no Ni_4Ti_3 detected in the unprocessed specimen, the formation of the metastable phase is a result of the highly nonequilibrium resolidification and is assumed to only be present in the melted and resolidified layer. In fact, a previous study performed by Birnbaum *et al.*[16] on completely melted amorphous NiTi films revealed the appearance of nucleated and grown highly textured [31–1] Ni_4Ti_3. The emergence of the [110] austenite peak, however, is believed to be due to the local stress relaxation caused by the melt and solidification process. Its appearance suggests a decrease in phase transformation temperatures, thus acting to stabilize the austenite at the expense of the [1–11] martensite. This further supports the mechanism proposed in Sec. IV as the peak intensity of the austenite peak also grows, accounting for a greater volume fraction, as energy density is increased.

Figure 10 shows the phase transformation temperatures as obtained from XRD spectra processed with varying energy density. The emergence and disappearance of the [110] austenitic peak were used to gauge the start and finish temperatures. It is seen that this occurs at successively lower temperatures until the [110] peak may be seen at room temperature (without any heating). This room temperature emergence is seen upon an incident laser energy density of 837 mJ/cm^2. Essentially what has happened is that the phase transformation temperature is dropping below room temperature, thus stabilizing the austenite and destabilizing

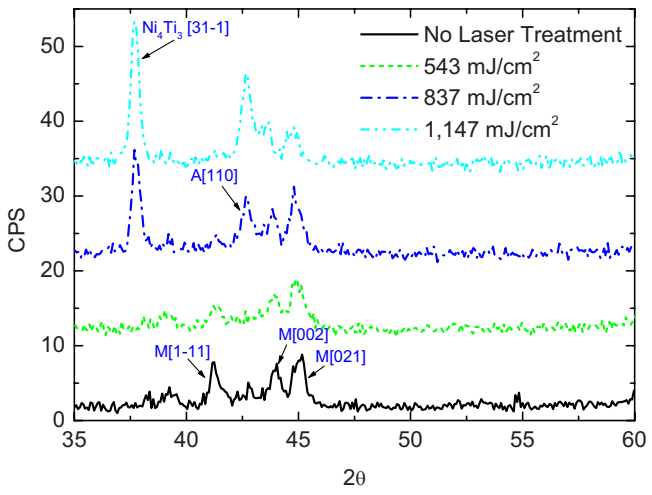

FIG. 9. (Color online) XRD spectra taken at room temperature revealing the phase(s) present as a function of laser energy density. Note the disappearance of the martensite [1–11] peak accompanied by the emergence of the austenite [110] and Ni_4Ti_3 [31–1] peaks.

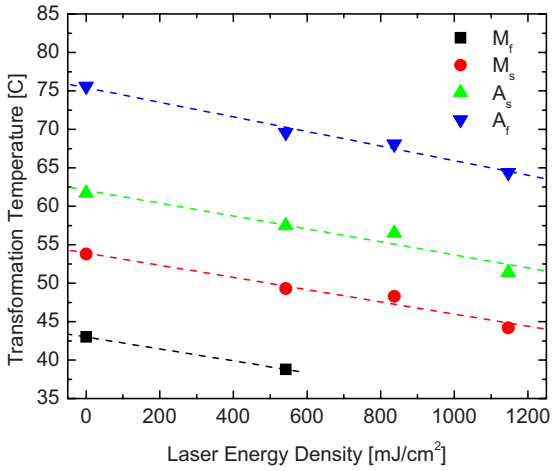

FIG. 10. (Color online) Martensitic phase transformation temperatures as a function of incident laser energy density. Note the monotonic decrease for all start and finish temperatures. Also note the fact that the martensitic finish temperatures for the 837 and 1147 mJ/cm^2 cases (not shown) drop below room temperature, explaining the residual austenite observed in Fig. 9.

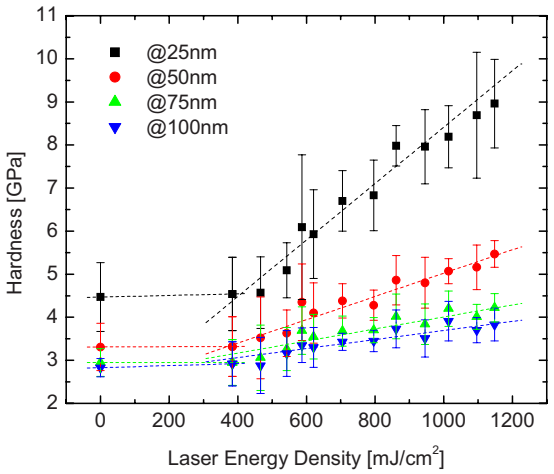

FIG. 11. (Color online) Plot of hardness as a function of incident laser energy density for 25, 50, 75, and 100 nm ultimate indentation depths.

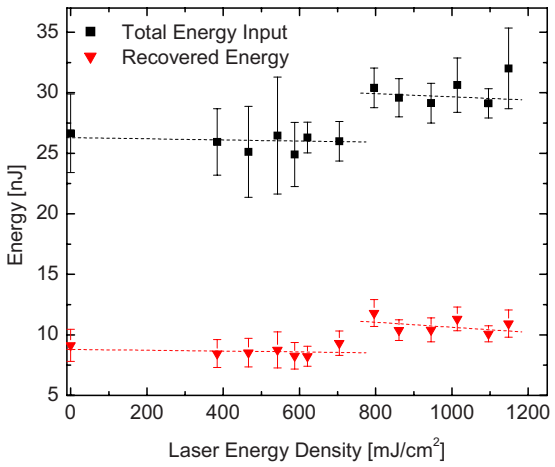

FIG. 12. (Color online) Total energy input upon indenting (100 nm ultimate depth) and recovered energy upon unloading as a function of incident laser energy density. Note the sudden increase in both the total energy required and recovered energy for an incident energy of 795 mJ/cm^2 corresponding with the emergence of austenite and the nonshape memory phase (Fig. 9).

the martensite. This observed decrease in phase transformation temperature is indeed consistent with the mechanism proposed in Sec. IV. This increased depth of melting and subsequent incremental drop in stress and concomitantly in martensitic phase transformation temperature.

C. Nanoindentation response

1. Mechanical properties

In addition to modifying the phase transformation temperatures, the room temperature mechanical response is altered as well. Nanoindentation has been utilized to characterize both the as-annealed film and laser processed film over an array of incident energies. Additionally, since the ultimate depth of melting is a function of the incident energy, the respective thicknesses of these two layers are also a function of the laser energy.

Figure 11 is a plot of hardness as a function of incident energy density for a series of indentation depths. Hardness is calculated as P_{ult}/A_p, where P_{ult} and A_p are the ultimate indentation load and the projected area of contact at that load for a Berkovich indenter. It is observed that hardness for all indentation depths remain initially unaffected by changes in energy density; however, at approximately 500 mJ/cm^2, the hardness values begin to rise for all indentation depths.

Upon increasing the incident laser energy above approximately 500 mJ/cm^2, monotonic increases in hardness are observed for a series of ultimate indentation depths (25, 50, 75, and 100 nm). Additionally, the hardness also decreases monotonically for increased indentation depths. This is observed in the nonlaser treated specimen as well, suggesting that this is due to size effects stemming from the presence of geometrically necessary dislocations.[25] However, in terms of the energy density dependence, several phenomena must be considered in order to explain the observed behavior.

The laser process results in a two layered structure. The load response of the nanoindenter is a composite response from both layers. Furthermore, all nanoindentation data presented are for probed depths of 100 nm or less. Fischer-Cripps[25] suggested that this is sufficiently shallow to ensure a film-dominated response for a 1 μm film thickness. Additionally, the location (in depth) of the interface between the two layers changes as a function of the incident fluence which results in an increased melted to unmelted thickness ratio. Thus the 25 nm response will become melted-layer dominated the quickest as the melt depth increases with laser energy density. This is manifested by an increased slope of the hardness as a function of laser fluence. This argument extends to the 50, 75, and 100 nm cases with continually decreasing respective slopes. Furthermore, the increase in hardness itself is due to both the stabilization of austenite due to a decreased phase transformation temperature and the appearance of the metastable phase as discussed in Sec. V B 2 and seen in Fig. 9. Austenite is reported to be significantly harder[26] and a previous study by Birnbaum *et al.*[17] reported an even higher hardness for the metastable phase as approximately 8 GPa which is also presumed to be present only in the melted layer.

2. Shape memory response

In addition to examining the traditional load response in terms of hardness, the nontraditional shape memory responses, namely, the SEs and SMEs, are also examined via the use of nanoindentation. Figure 12 is a plot of the total energy input upon indenting and energy recovered upon unloading a function of laser energy. All data presented in Fig. 12 were obtained from 100 nm indentation depths at room temperature. It is seen that both the total and recovered energies remain fairly constant until a step increase is observed for both at approximately 800 mJ/cm^2.

Following the treatment given by Birnbaum *et al.*,[17] for austenitic (superelastic) shape memory alloys (SMA's), upon loading, energy is stored elastically and dissipated via plastic slip and the stress induced phase transformation. Upon unloading, energy is recovered elastically as well as through the reverse transformation. For martensitic SMAs, energy is also stored elastically and dissipated via plastic deformation a twin reorientation. Upon unloading, only the elastically

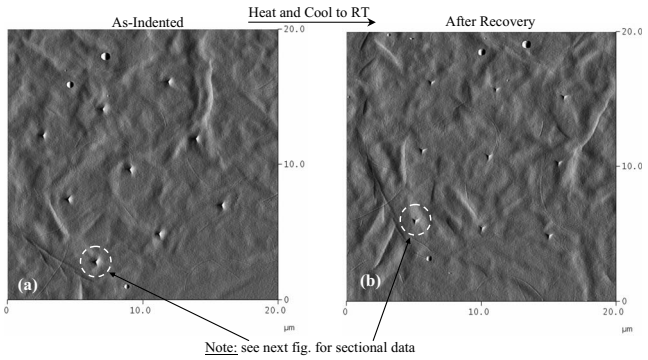

FIG. 13. (a) Representative AFM image of room temperature as-indented martensitic film. (b) AFM image after heating revealing depth recovery due to the SME.

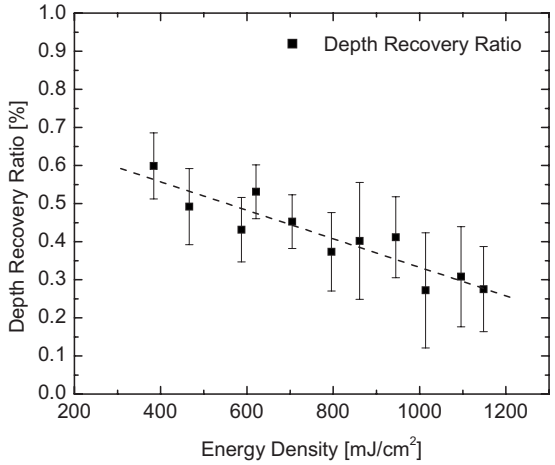

FIG. 15. Depth recovery ratio upon heating as a function of incident energy density. Note the monotonic decrease due to the stabilization of austenite as well as the appearance of the nonshape memory phase.

stored energy is recovered. It is assumed that the metastable phase follows the more traditional elastic-plastic response.

Examining the XRD spectra in Fig. 9, the presence of austenite and the metastable phase is detected at room temperature at approximately the same energy density as the step change is observed in total and recovered energies. This stems from austenite recovering both elastic *and* superelastic deformations. Additionally, the increased hardness associated with austenite and the metastable phases also results in larger ultimate loads (for a given depth) and therefore enhanced energy input as well.

In addition to responses due to the SE in terms of recoverable energy, the SME may be characterized via an examination of the recoverable depth upon heating of the film. As explained above, martensitic films do not recover the deformation from twin reorientation upon unloading. However, this deformation *is* recovered upon heating due to the SME. The experiment is performed as follows. Nanoindentation is performed to an ultimate depth of 100 nm. The subsequent residual impressions are then quantified via atomic force microscopy (AFM). The film is then heated to above the austenitic finish temperatures and allowed to cool to room temperature. The residual impressions are then scanned again with an AFM.

Figures 13(a) and 13(b) are AFM micrographs of the film as indented and after having been heated and then cooled to room temperature. The residual imprints of the as-indented film are due to both true plastic deformation and twin reorientation. Upon heating, the deformation due to twin reorientation is recovered, but the plastic strains of course remain. Figures 14(a) and 14(b) are cross sections of an indent before and after heating. It is clearly seen that a significant portion of the as-indented depth is recovered upon heating due to the SME. Figure 15 is a plot of the depth recovery ratio,

$$d^{\mathrm{rec}} = \frac{d_i - d_f}{d_i}, \tag{7}$$

where d_i is the as-indented depth and d_f is the depth after heating. A monotonic decrease in d^{rec} as a function of laser energy is seen. This is due to two major factors. The first is the presence of the metastable phase which is not associated with strain recovery via the SME. The other is the continual decrease in phase transformation temperature resulting in the stabilization of austenite at the expense of martensite. Austenite is also not associated with depth recovery due to heating, but as explained above does result in enhanced strain recovery due to the SE upon unloading.

VI. CONCLUSION

In conclusion, it has been demonstrated that pulsed, melt-mediated laser irradiation within the partial melting regime is in fact capable of modifying aspects of the thermodynamic, mechanical, and shape memory responses of NiTi

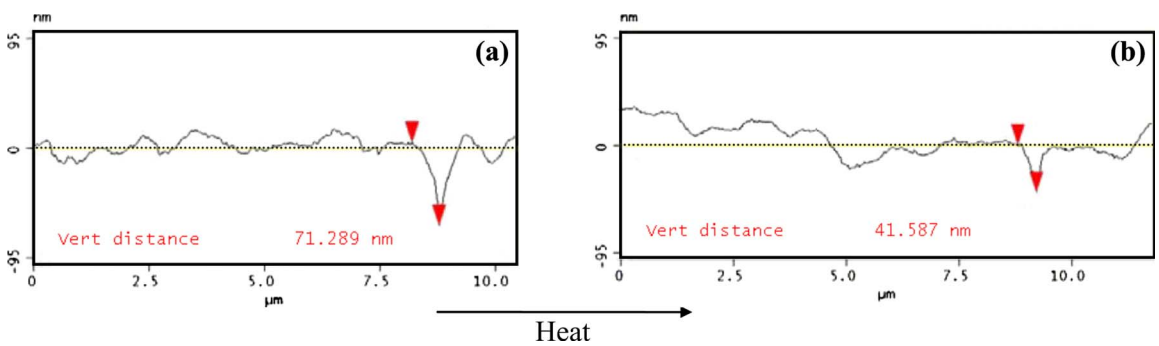

FIG. 14. (Color online) (a) Representative sectional analysis from AFM data from indent prior to heating. (b) Sectional analysis from AFM data after heating revealing depth recovery due to the SME.

thin films. More specifically, martensitic phase transformation temperature decreases with increasing laser energy density. Accompanying mechanical and shape memory responses of laser processed films are also characterized via nanoindentation. It was shown that recoverable energy upon unloading is enhanced with increases in incident laser energy via the stabilization of austenite and thus the superelastic response. A concomitant decrease in the depth recovery ratio is also observed with increasing laser fluence due to the destabilization of martensite, and thus decreased magnitudes of strain that may be accommodated via detwinning. Furthermore, a stress based mechanism explaining the observed thermodynamic and mechanical phenomena is proposed. Specifically, increases in laser fluence (melt depth) result in decreases in film stress giving rise to the change in material response. As this process has been shown to successfully alter aspects of the film's shape memory response, it may now be applied in fabricating monolithic, functionally graded microscale devices.

ACKNOWLEDGMENTS

The authors would like to acknowledge Professor James S. Im of the Columbia University, Materials Science Department for allowing the use of his laser facilities as well as valuable advice and discussion. The authors would also like to thank Professor Ainissa Ramirez and Dr. Xu Huang for their role in thin film deposition.

[1]K. P. Mohanchandra, K. K. Ho, and G. P. Carman, Mater. Lett. **62**, 3481 (2008).
[2]F. Ciabattari, F. Fuso, and E. Arimondo, Appl. Phys. A: Mater. Sci. Process. **64**, 623 (1997).
[3]A. Ishida, A. Takei, and S. Miyazaki, Thin Solid Films **228**, 210 (1993).
[4]M. A. Arranz and J. M. Riveiro, J. Magn. Magn. Mater. **290–291**, 865 (2005).
[5]S. Miyazaki and A. Ishida, Mater. Sci. Eng., A **273–275**, 106 (1999).
[6]T. Lehnert, S. Crevoiserat, and R. Gotthardt, J. Mater. Sci. **37**, 1523 (2002).
[7]C. L. Shih, B. K. Lai, H. Kahn, S. M. Phillips, and A. H. Heuer, J. Microelectromech. Syst. **10**, 69 (2001).
[8]D. Shin, D. G. Lee, K. P. Mohanchandra, P. Gregory, and G. P. Carman, Sens. Actuators, A **130–131**, 37 (2006).
[9]D. P. Cole, H. A. Bruck, and A. L. Roytburd, J. Appl. Phys. **103**, 064315 (2008).
[10]R. M. S. Martins, N. Schell, A. Mücklich, H. Reuther, M. Beckers, R. J. C. Silva, L. Pereira, and F. M. Brazfernandes, Appl. Phys. A: Mater. Sci. Process. **91**, 291 (2008).
[11]Y. Fu and H. Du, Mater. Lett. **57**, 2995 (2003).
[12]I.-J. Kim and H.-W. Lee, Scr. Mater. **44**, 525 (2001).
[13]X. Wang, Y. Bellouard, and J. J. Vlassak, Acta Mater. **53**, 4955 (2005).
[14]Y. Bellouard, T. Lehnert, J.-E. Bidaux, T. Sidler, R. Clavel, and R. Gotthardt, Mater. Sci. Eng., A **273–275**, 795 (1999).
[15]Q. He, M. H. Hong, W. M. Huang, T. C. Chong, Y. Q. Fu, and H. J. Du, J. Micromech. Microeng. **14**, 950 (2004a).
[16]A. J. Birnbaum, U. J. Chung, X. Huang, A. G. Ramirez, S. Polvino, and Y. L. Yao, Proceedings of ICALEO-Laser Materials Processing, 2007 (unpublished), pp. 98–107.
[17]A. J. Birnbaum, U.-J. Chung, X. Huang, J. S. Im, A. G. Ramirez, and Y. L. Yao, J. Appl. Phys. **105**, 073502 (2009).
[18]X. Wang, Y. Bellouard, Z. Xue, and J. Vlassak, Appl. Phys. A: Mater. Sci. Process. **90**, 689 (2008).
[19]P. Wollants, M. D. Bonte, and J. R. Roos, Z. Metallkd. **70**, 113 (1979).
[20]Y. Fu and H. Du, Surf. Coat. Technol. **153**, 100 (2002).
[21]Y. Q. Fu, S. Zhang, M. J. Wu, W. M. Huang, H. J. Du, J. K. Luo, A. J. Flewitt, and W. I. Milne, Thin Solid Films **515**, 80 (2006).
[22]D. S. Grummon, J. Zhang, and T. J. Pence, Mater. Sci. Eng., A **273–275**, 722 (1999).
[23]J. J. Gill, K. Ho, and G. P. Carmen, J. Microelectromech. Syst. **11**, 68 (2002).
[24]T. Wu, B. Jiang, X. Qi, Y. Liu, D. Xu, and L. Wang, Mater. Trans., JIM **43**, 566 (2002).
[25]A. C. Fischer-Cripps, *Nanoindentation*, 2nd ed. (Springer-Verlag, New York, 2004).
[26]G. Satoh, A. J. Birnbaum, and Y. L. Yao, Proceedings of the ICALEO, 2008.